OPEN

Correspondence and
requests for materials
should be addressed to
G.V.A. (astakhov@
physik.uni-
wuerzburg.de) or V.D.
(dyakonov@physik.
uni-wuerzburg.de)

Magnetic field and temperature sensing with atomic-scale spin defects in silicon carbide

H. Kraus[1], V. A. Soltamov[2], F. Fuchs[1], D. Simin[1], A. Sperlich[1], P. G. Baranov[2], G. V. Astakhov[1] & V. Dyakonov[1,3]

[1]Experimental Physics VI, Julius-Maximilian University of Würzburg, 97074 Würzburg, Germany, [2]Ioffe Physical-Technical Institute, 194021 St. Petersburg, Russia, [3]Bavarian Center for Applied Energy Research (ZAE Bayern), 97074 Würzburg, Germany.

Quantum systems can provide outstanding performance in various sensing applications, ranging from bioscience to nanotechnology. Atomic-scale defects in silicon carbide are very attractive in this respect because of the technological advantages of this material and favorable optical and radio frequency spectral ranges to control these defects. We identified several, separately addressable spin-3/2 centers in the same silicon carbide crystal, which are immune to nonaxial strain fluctuations. Some of them are characterized by nearly temperature independent axial crystal fields, making these centers very attractive for vector magnetometry. Contrarily, the zero-field splitting of another center exhibits a giant thermal shift of -1.1 MHz/K at room temperature, which can be used for thermometry applications. We also discuss a synchronized composite clock exploiting spin centers with different thermal response.

N anoscale magnetic field and temperature sensing based on quantum properties of the nitrogen-vacancy (NV) defect in diamond[1] has been proposed[2–5] and demonstrated at ambient conditions[6–8]. This sensing technique can potentially allow for monitoring neuron activity[9], imaging of single proton spins in complex molecular systems[10,11] and measuring the heat produced by chemical reactions inside living cells[12,13]. The principle of sensing is based on the optical readout of the spin resonance frequency subject to the crystal field D and magnetic field B.

These successful experiments have stimulated the search for other solid-state spin systems with similar abilities. Atomic-scale defects in silicon carbide (SiC) are attractive in this respect. Apart from the obvious technological opportunities due to the well-developed device fabrication protocols in SiC, these defects reveal favourable optical and radio frequency (RF) spectral ranges for their control. Namely, (i) they are optically active in the near infrared, characterised by a deep tissue penetration and a weak absorption in optical glass fibers. And (ii) they can be controlled by the MHz RF-fields, used in standard magnetic resonance imaging systems. Because of about 250 SiC polytypes are known, there should exist more than thousand different spin defects in SiC with distinct characteristics[14,15]. One can select defects with the most suitable properties for a concrete task, which is not possible for one universal sensor.

Here, we identify separately addressable spin centers within the primary intrinsic defects in 6H-SiC and 4H-SiC. Some of these half-integer spin ($S = 3/2$) centers are insensitive to nonaxial strain as a consequence of the Kramers degeneracy theorem and reveal within our accuracy temperature independent crystal field. Thermal/strain fluctuations may limit the magnetometry performance. In particular, thermal fluctuations lead to fluctuations of the spin resonance frequency because D is generally a function of temperature (T). The NV defect demonstrates the thermal shift of the spin resonance frequency $\beta = -74$ kHz/K[16], and temperature fluctuations of $1°C$ results in a magnetic field uncertainty of a few μT. By stabilizing temperature and using advanced measurement protocols in a bias magnetic field, this uncertainty can be significantly reduced[17], while in case of SiC this is already the intrinsic property.

On the other hand, a large thermal shift is necessary for temperature sensing. We also identify spin-3/2 centers, demonstrating giant thermal shifts up to $\beta = -1.1$ MHz/K at ambient conditions. This is 14 times larger than that for the NV defect and hence can potentially be used to enhance the thermometry sensitivity.
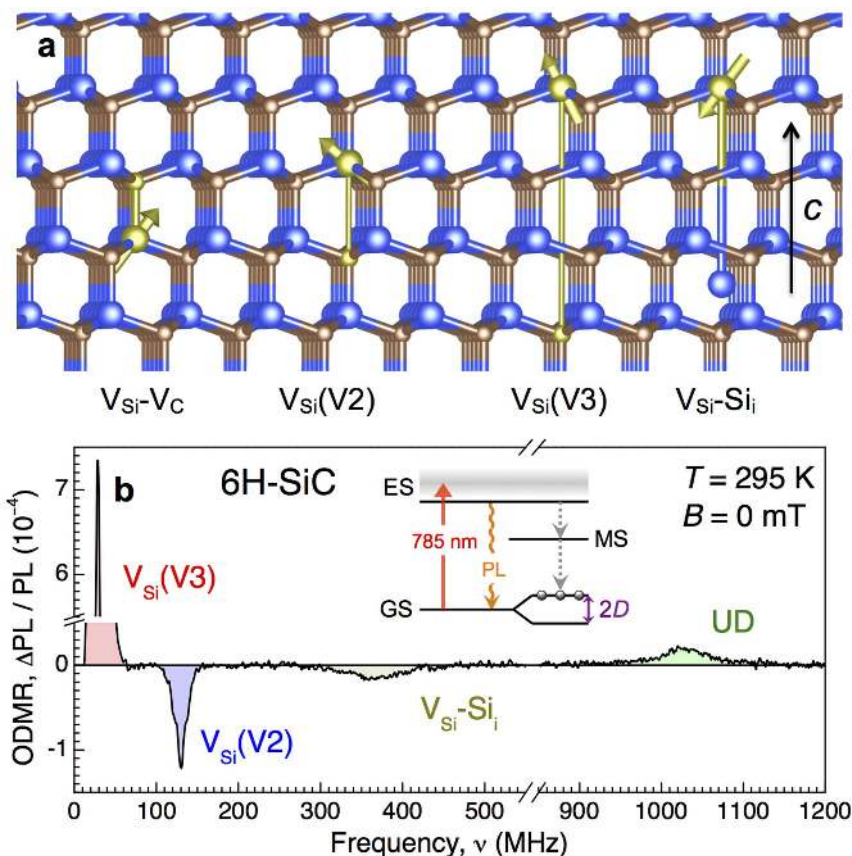
Figure 1 | Optical detection of spin defects in 6H-SiC. (a) Crystallographic structures of the Schottky [V_{Si}-V_C, V_{Si}(V2), V_{Si}(V3)] and Frenkel (V_{Si}-Si_i) defects. All the defects have the symmetry axis oriented along the *c*-axis of the crystal lattice. (b) Room-temperature zero-field ODMR spectrum. Inset: optical pumping scheme of spin defects.

I. Room-temperature ODMR of intrinsic defects in 6H-SiC

The Schottky and Frenkel defects are the primary stoichiometric defects in solids. A divacancy (V_{Si}-V_C)–consisting of chemically bound silicon vacancy (V_{Si}) and carbon vacancy (V_C)–is an example of a Schottky defect in SiC [Fig. 1(a)] being extensively investigated[18–21]. Another example of a Schottky defect is an isolated silicon vacancy[18,22–28] perturbed by the nearest carbon vacancy along the *c*-axis of the SiC lattice[15]. There are several possible configurations and two of them are labeled in Fig. 1(a) as V_{Si}(V2) and V_{Si}(V3). Frenkel defects have also been identified in SiC and one of such defects–a silicon vacancy and a corresponding interstitial Si atom located at a distance of 6.5 Å along the *c*-axis (V_{Si}-Si_i)[29]–is shown in Fig. 1(a).

A common feature of these defects in SiC is that they have a high-spin ground state[19,29]. The corresponding spin Hamiltonian is written in the form

$$\mathcal{H} = g_e \mu_B \mathbf{BS} + D(T)\left[S_z^2 - S(S+1)/3\right].\tag{1}$$

Here, $g_e \approx 2.0$ is the electron g-factor, μ_B is the Bohr magneton and S_z is the projection of the total spin S on the symmetry axis of the defect (in case of the defects considered here it coincides with the *c*-axis of SiC). Without external magnetic field ($B = 0$) the ground state is split due to the crystal field D and for $S = 3/2$ the zero-field splitting (ZFS) between the $m_s = \pm 1/2$ and $m_s = \pm 3/2$ sublevels is equal to $2D$ [the inset of Fig. 1(b)]. Remarkably, the zero-field splitting is an individual fingerprint for each defect. In table I we summarize the ZFS values for different intrinsic defects in the most commonly encountered polytype 6H-SiC.

We now demonstrate, using optically detected magnetic resonance (ODMR) technique, that defect spins in 6H-SiC can be initialized and read out at ambient conditions, which is the basis for various sensing applications. Optical excitation with 785 nm followed by spin-dependent recombination through the metastable state (MS) results in a spin polarization of the defect ground state [the inset of Fig. 1(b)]. On the other hand, photoluminescence (PL) rates from the excited state (ES) to the ground state (GS) involving different spin sublevels are different. When a resonance RF equal to the ZFS is applied ($\nu_0 = 2D/h$ for $S = 3/2$), it induces magnetic dipole transitions between the spin-split sublevels resulting in a change of the photoluminescence intensity (ΔPL). Since single photons emitted by a single defect can be detected, this ODMR technique is now a standard method to probe single NV spins in diamond[1], which has the resonance frequency around $\nu_0 = 2.87$ GHz.

In order to probe spin defects in SiC we have extended the RF spectral range from a few GHz down to a few tens of MHz, usually assigned for nuclear magnetic resonance experiments. Figure 1(b) shows a typical ODMR spectrum, i.e., relative change of the photoluminescence intensity ΔPL/PL as a function of applied RF. Two spin resonances at $\nu_0 = 28$ MHz and $\nu_0 = 128$ MHz agree well with ZFS of the silicon vacancy defects V_{Si}(V3) and V_{Si}(V2), respectively (table I). Another spin resonance is observed at $\nu_0 = 367$ MHz

Table I | Zero-field splitting (spin resonance frequency) of intrinsic defects in 6H-SiC

V_{Si}-V_C divacancy	V_{Si}(V2) "hexagonal"	V_{Si}(V3) "cubic"	V_{Si}-Si_i Frenkel pair
1.28 GHz	127 MHz	27 MHz	408 MHz
Ref. 19 $T = 2$ K	Refs. 23, 27 $T = 2, 50$ K		Ref. 29 $T = 300$ K
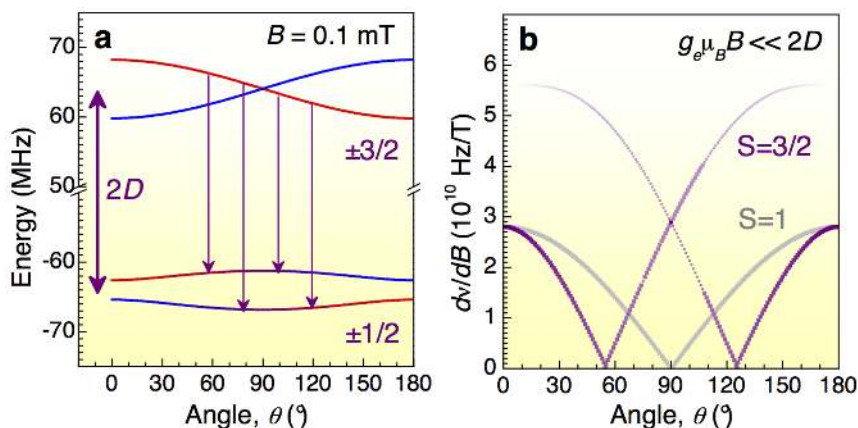
Figure 2 | Vector magnetometry. (a) Zeeman splitting of the $\pm 3/2$ (upper) and $\pm 1/2$ (lower) spin sublevels as a function of the angle θ between magnetic field $B = 0.1$ mT and the defect symmetry axis ($2D = 128$ MHz). The arrows indicate four possible RF-induced transitions. (b) Comparison of the relative shifts of the spin resonance frequencies dv/dB as a function of θ for $S = 1$ and $S = 3/2$.

and we ascribe it to the Frenkel pair V_{Si}-Si_i (table I). A discrepancy of 10% can be explained by the strong dependence of its ZFS on temperature and laser power, as described later in this work (see also Supplemental Material). Finally, we discuss the origin of the spin resonance at $v_0 = 1.03$ GHz. We find that this spin resonance is strongly temperature dependent–$D(T)$ is discussed later in detail– and at $T = 10$ K we measure the zero-field splitting to be $v_0 = 1.22$ GHz. This agrees reasonably well with ZFS of the divacancy V_{Si}-V_C (table I). On the other hand, we register PL up to 1050 nm, but the V_{Si}-V_C PL has maximum above 1100 nm[20]. We would like to mention that the magnetic field dependencies (presented later) unambiguously indicate $S = 3/2$ for this defect, while in the earlier studies the $S = 1$ ground state of the divacancy was assumed[19]. For this reason we label it as unidentified defect (UD) in all figures, indicating that its origin should be carefully examined.

First, as a characteristic example, we consider theoretically the Zeeman splitting of the V_{Si}(V2) spin sublevels for different orientations (given by the polar angle θ) of a weak magnetic field $B \ll 2D/g_e\mu_B$ [Fig. 2(a)]. The V_{Si}(V2) defect has spin $S = 3/2$ ground state[15,22,24] and the upper $m_s = \pm 3/2$ spin sublevels are split as $\pm\frac{3}{2}g_e\mu_B B \cos\theta$. Interestingly, the lower $m_s = \pm 1/2$ spin sublevels are mixed due to the perpendicular-to-the-symmetry-axis field component and split differently as $\pm\frac{1}{2}g_e\mu_B B(1 + 3\sin^2\theta)^{1/2}$, which results in four possible RF-induced transitions. We obtain the probability of these transitions [color-coded in Fig. 2(b)] as

$$W_{jk} \sim |\langle j|\mathbf{B}_1\mathbf{S}|k\rangle|^2, \qquad (2)$$

where $|j\rangle$, $|k\rangle$ are the eigenstates of (1) and $B_1 \perp c$ is the driving RF field.

Figure 2(b) compares the relative shifts of the spin resonance frequency dv/dB depending on the magnetic field orientation for $S = 1$ and $S = 3/2$. In case of a spin-1 system (i.e., the NV defect) it follows $|g_e\mu_B \cos\theta/h|$ (h is the Planck constant) and tends to zero for $B \perp c$ ($\theta = 90°$). Therefore, using a single (or equally oriented) spin-1 defect(s) the field projection on the defect symmetry axis $B_z = B\cos\theta$ rather than the absolute value is detected. In fact, due to the presence of the nuclear spin bath, the NV spin-echo decay curve contains characteristic "collapses and revivals" from which the total magnetic field can be determined[30]. However, the nuclear gyromagnetic ratio is much smaller (by a factor of 0.0003 for ^{13}C) than that of electron, making this method less sensitive. Furthermore, this method is not applicable for isotopically purified crystals, providing the highest sensitivity. In contrast, in case of a spin-3/2 system there are two pairs of resonances. Therefore, from the comparison of the

relative ODMR frequencies and amplitudes both the absolute value B and its orientation with respect to the defect symmetry axis can be reconstructed.

In order to demonstrate this advantage of the spin-3/2 defects in SiC for magnetic sensing applications it is necessary to ascertain their symmetry axes. This can be done in high magnetic fields $B \gg 2D/g_e\mu_B$. In this case, a pair of spin resonances should be observed for each spin defect, the separation between those being a function of θ. We have performed this experiment in the X-Band at a fixed frequency $v = 9.4$ GHz while sweeping the magnetic field and an ODMR spectrum obtained for $B||c$ is shown in Fig. 3(a). Indeed, four pairs of spin resonances from four distinct spin defects are observed, in accord with four lines in the zero-field ODMR spectrum of Fig. 1(b). The resonance magnetic fields $B_\pm$ related to each pair are presented in Fig. 3(b) as a function of the angle between the field direction and the c-axis.

According to spin Hamiltonian (1), the difference between these fields is given by

$$\Delta B = B_+ - B_- = \frac{2D(T)}{g_e\mu_B}\left(3\cos^2\theta - 1\right). \qquad (3)$$

As Eq (3) describes the experimental data quite well [Fig. 3(b)], one immediately concludes that all the defects under consideration are in line with the c-axis, as also depicted in Fig. 1(a). Furthermore, for $B||c$ ($\theta = 0°$) ZFS can independently be measured[27] as $2D = g_e\mu_B\Delta B/2$ and from the comparison with the zero-field data of Fig. 1(b) all the resonances in Fig. 3 are unambiguously assigned.

Having established the orientation of the spin defects in our 6H-SiC sample, we apply a weak magnetic field $B = 2.2$ mT perpendicular to the defect symmetry axis ($\theta = 90°$) [Fig. 4(a)]. In this configuration the difference between different spin systems is most pronounced [see Fig. 2(b)]. For a spin-1 defect such oriented weak magnetic fields should have no effect. In contrast, we observed large Zeeman splittings for all four ODMR lines [symbols Fig. 4(b)]. The experimental data are perfectly described by the spin Hamiltonian (1) with $S = 3/2$ and corresponding transition rates of Eq. (2), as shown by the solid lines in Fig. 4(b). For comparison, the calculations with $S = 1$ are shown by the dotted lines. Remarkably, for V_{Si}(V2) and especially for V_{Si}(V3) the magnetic field behavior is not linear because the Zeeman splitting in a magnetic field of a few mT is comparable or larger than ZFS in these silicon vacancy defects, which results in the intermixing of all four spin sublevels. According to the magnetic field dependencies of Fig. 4(b), all defects under consideration have the $S = 3/2$ ground state. This is in agreement with the
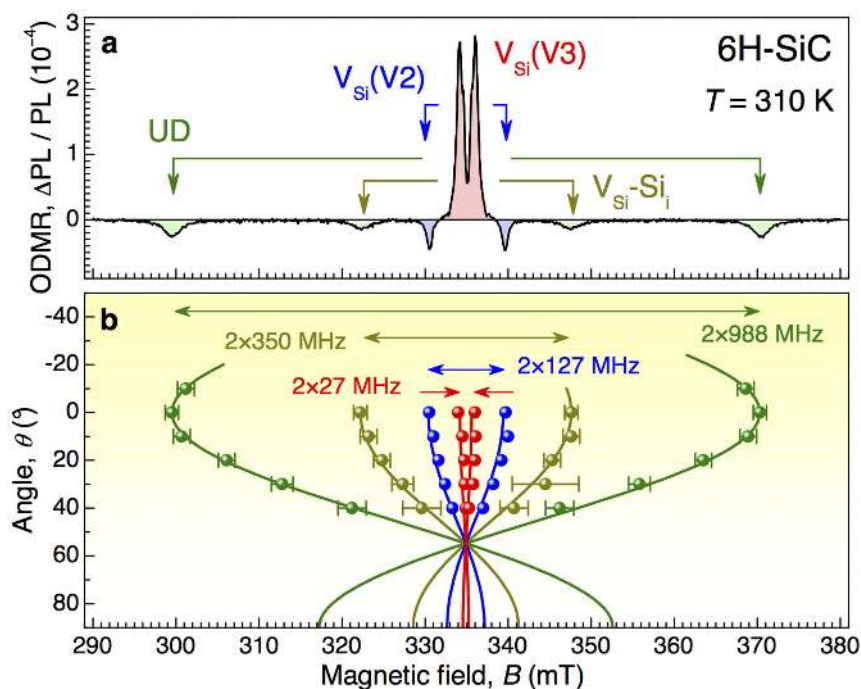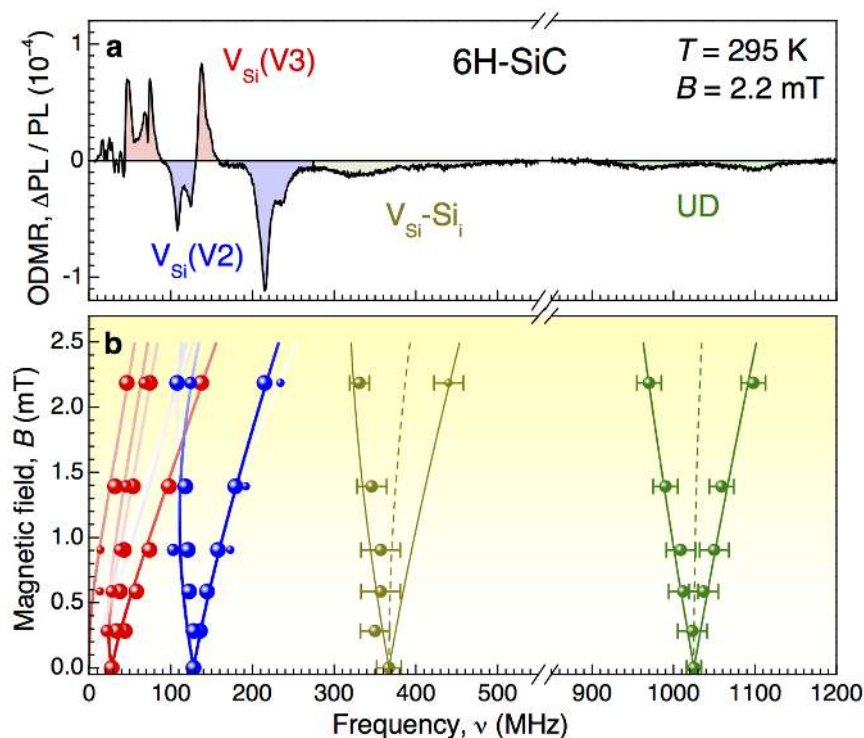
Figure 3 | Axial symmetry of spin defects in 6H-SiC. (a) Room-temperature ODMR spectrum in the X-band ($\nu = 9.4$ GHz) as a function of magnetic field $B\|c$. (b) ODMR frequencies for different angles between the magnetic field B and the c-axis of 6H-SiC. Experimental data are shown by symbols, the solid lines correspond to the calculations to Eq (3).

earlier ascertained spin structure of the V_{Si} defects[15] and with the model of the V_{Si}-Si_i Frenkel pairs[29].

We now discuss the effect of strain. In case of $S = 1$ spin system, as the NV defect in diamond and the divacancy in SiC, the local strain lifts up the degeneracy of the $m_s = \pm 1$ spin sublevels even without external magnetic field. It is described by an additional term $E\left(S_x^2 - S_y^2\right)$ in the spin Hamiltonian, where E is the transverse ZFS parameter. This may limit the magnetometry sensitivity because the spin-splitting in external magnetic field for $E \neq 0$ is described

Figure 4 | Effect of external magnetic field in 6H-SiC. (a) Room-temperature ODMR spectrum obtained in a magnetic field $B = 2.2$ mT. (b) ODMR frequencies as a function of magnetic field. Experimental data are shown by symbols, the solid and dotted lines correspond to the calculations for $S = 3/2$ and $S = 1$, respectively. In all panels $\mathbf{B} \perp c$.
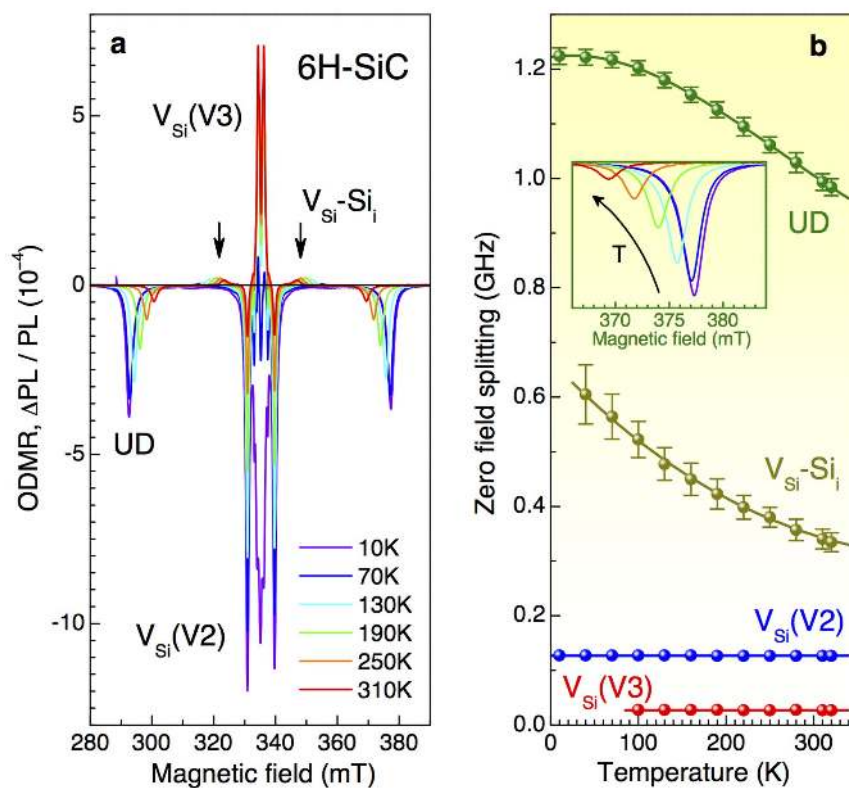
Figure 5 | Temperature effect in 6H-SiC. (a) ODMR spectra in the X-band (v = 9.4 GHz) recorded at different temperatures. (b) Zero-field splitting 2D for different spin defects as a function of temperature. The solid lines are third order polynomial fits. Inset: The same as (a), but rescaled to highlight a strong UD temperature dependence.

by $\sqrt{(g_e\mu_B B_z)^2 + E^2}$, i.e., the relative shift of the spin resonance frequency is quadratic rather than linear for small B. By improving the quality of bulk diamond material, the parameter E can be reduced below 1 MHz and further eliminated in a small bias magnetic field. However, magnetic fields may lead to additional inhomogeneity, which is in some experiments unwanted. Furthermore, in nanodiamonds, which are very interesting for bio-sensing, strain is usually present and the transverse ZFS parameter can be as large as E = 20 MHz[31]. The situation is qualitatively different for half-integer spin systems, like spin defects with S = 3/2. According to the Kramers theorem, the double degeneracy of the $m_s = \pm 1/2$ and $m_s = \pm 3/2$ states can only be lifted up by an external magnetic field, meaning that essentially E = 0. This makes these defects (in particular, silicon vacancies in SiC) more robust against strain fluctuations. Excitons and trions[32] are a well-known example of this consequence of the Kramers degeneracy theorem in solid-state system. Excitons (with integer angular momentum J = 1) demonstrate a fine structure splitting in quantum dots. It is caused by local strain due to lattice mismatch between the material of the quantum dot and the barrier. On the other hand, the trions (with half-integer angular momentum J = 3/2) reveal no fine structure splitting under the same strain conditions[33].

In order to examine the effect of temperature fluctuations, we have measured ODMR spectra in the temperature range from 10 to 320 K [Fig. 5(a)]. The experiment is performed in the X-band and D for each defect is determined using Eq. (3). As one can see from Fig. 5(b) the parameter D of the $V_{Si}(V2)$ and $V_{Si}(V3)$ defects is temperature independent within the accuracy of our experiment (a few kHz/K). This is an additional strong argument to use these defects for magnetometry.

In contrast to $V_{Si}(V2)$ and $V_{Si}(V3)$, for the Frenkel pair V_{Si}-Si_i we observe a reduction of its ZFS of ca. 50%, from 0.6 down to 0.3 GHz

when the temperature increases from 10 to 320 K [Fig. 5(b)]. The corresponding temperature dependence is well described by a third order polynomial $2D(T) = a_0 + a_1 T + a_2 T^2 + a_3 T^3$ with a_0 = (667 ± 4) MHz, a_1 = (−1.7 ± 0.1) MHz/K, a_2 = (2.3 ± 0.8) × 10^{-3} MHz/K², and a_3 = (−8 ± 15) × 10^{-7} MHz/K³. The defect with the largest ZFS (labeled as UD in Fig. 5) has a slightly weaker temperature dependence (17% relative reduction of D) but reveals the strongest thermal shift $2dD/dT$ at room temperature [the inset of Fig. 5(b)]. From the polynomial fit with a_0 = (1222 ± 2) MHz, a_1 = (2.4 ± 0.4) × 10^{-1} MHz/K, a_2 = (−5.2 ± 0.3) × 10^{-3} MHz/K², and a_3 = (6.5 ± 0.5) × 10^{-6} MHz/K³ we find β = $2dD/dT$ = −1.1 MHz/K at T = 300 K. This value is 14 times larger than the thermal shift of the NV defect in diamond[16].

II. Intrinsic defects in 4H-SiC and magnetic field sensing

We also observe very similar behaviour in 4H polytype of SiC, which can be grown of high quality. Figure 6(a) shows a room-temperature ODMR spectrum of 4H-SiC, obtained in the X-Band spectrometer. Following the angle dependencies presented in Fig. 6(b) we ascribe the ODMR lines to the silicon vacancy $V_{Si}(V2)$ (with ZFS of 67 MHz) and the Frenkel pair V_{Si}-Si_i (with ZFS of 408 MHz)[23,27,29].

We now concentrate on the ODMR spectra of the $V_{Si}(V2)$ defect in zero and weak bias magnetic fields [Fig. 7(a)]. In zero magnetic field, the ODMR line has maximum around $v_0 \approx 70$ MHz [Fig. 7(b)]. Upon application of a magnetic field along the c-axis ($\theta = 0°$), the ODMR line is split and one observes two resonances [Fig. 7(a)]. They shift linear with magnetic field as $v_B = |v_0 \pm g_e\mu_B B/h|$ [Fig. 7(b)], in accord to Hamiltonian (1) for $\mathbf{B} \| c$. From the linear fit we find the $V_{Si}(V2)$ ZFS in our crystal with higher accuracy v_0 = 70.2 ± 0.3 MHz.

In our earlier studies we have reported that the ODMR linewidth in SiC strongly depends on the RF power[15]. Therefore, to achieve the narrowest linewidth we use the lowest RF power, which still provides
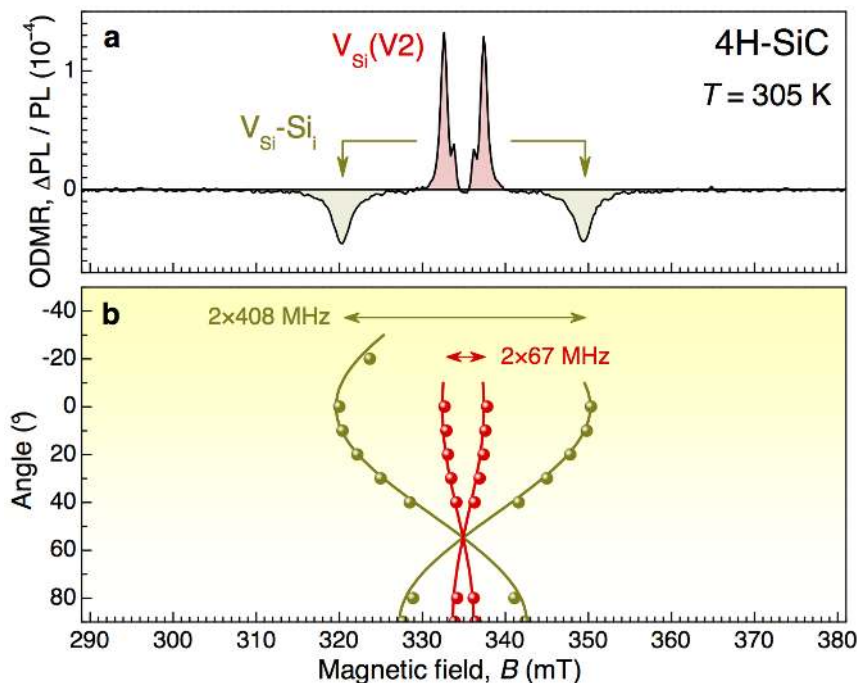
Figure 6 | Room-temperature ODMR in 4H-SiC. (a) An ODMR spectrum in the X-band ($v = 9.4$ GHz) as a function of magnetic field $\mathbf{B} || c$. (b) ODMR frequencies for different angles between the magnetic field B and the c-axis. Experimental data are shown by symbols, the solid lines correspond to the calculations to Eq (3).

a reasonable signal-to-noise ratio. Additionally, we apply a small bias magnetic field of 3.5 mT to eliminate the broadening due to environment magnetic fields. The result is presented in Fig. 7(c) and can be well fitted to

$$\frac{\Delta \text{PL}}{\text{PL}}(v) = \sum_{n=0,1,2} \frac{\Gamma_n}{[2\pi T_2^* (v_B \pm nA_{\text{Si}}/2 - v)]^2 + 1}. \qquad (4)$$

Here, A_{Si} is the hyperfine constant describing the interaction $\mathcal{H} = \mathbf{IAS}$ with the next-nearest-neighbor (NNN) ^{29}Si ($I = 1/2$) nuclear spins. We find $A_{\text{Si}} = 9.1 \pm 0.2$ MHz, which is comparble with the earlier reported value[23]. The relative amplitudes of the peaks $\Gamma_0 : \Gamma_1 : \Gamma_2$ is given by the probability to find n spin-active ^{29}Si isotopes among the 12 Si NNN. We find $0.89 \times 10^{-4} : 0.24 \times 10^{-4} : 0.36 \times 10^{-5}$, which are close to the ratios expected for the natural abundance of ^{29}Si (4.7%).

The resonance linewidth in Fig. 7(c) is inversely proportional to the inhomogeneous spin coherence time, which is $T_2^* = 120$ ns according fit to Eq. (4). The accuracy to measure the relative change of the frequency (δv) is given by the maximum value of the derivative $(\delta \Gamma / \delta v)_{max} = \pi T_2^* \Gamma_0$. With the root-mean-square deviation $\delta \Gamma = 3.5 \times 10^{-6}$ [as in Fig. 7(c)] we obtain $\delta v = 100$ kHz. Taking into account the integration time of 8 s per point, this corresponds to the magnetic field sensitivity $\delta B = 10 \mu\text{T}/\sqrt{\text{Hz}}$. The sensitivity can be improved by increasing of T_2. It is limited by the spin-lattice relaxation time, which is $T_1 = 100 \mu s$[26] for V_{Si} in SiC and can be achieved using spin-echo techniques. Further improvement by approximately an order of magnitude should also be possible in isotopically purified ^{28}Si^{12}C, as was proposed recently[27]. For instance, the record spin coherence time of the NV defect in ^{12}C-diamond is $T_2 = 1.8$ ms[34]. In order to compare the sensitivity of the V_{Si} defect with the sensitivity of the NV defect, we first estimate the product of the overall detection efficiency ($\mathcal{C}$) and the number of the V_{Si}(V2) defects (N) in our experiments, by taking into account the signal level (ca. 10 nW) and the PL lifetime (6 ns, ref. 35). We then estimate the expected sensitivity for optimized samples to be on the order of magnitude $\delta B = 10 \text{ nT}/\sqrt{\mathcal{C}N \cdot \text{Hz}}$.

Our experiments have been performed on an ensemble of defects. Very recently, the detection of some single defect centers in SiC has been reported[36], and we believe that the same approach can be used to isolate single V_{Si}-related defects. An important issue in this case is the ODMR contrast. It increases with RF power and we observe $\Gamma_0 = 0.11\%$ for RF power of 36 dBm. This may lead to some limitations compared to single NV defects with larger ODMR contrast ($\Gamma_0 \sim 10\%$), such as a requirement of longer integration time to achieve the equal sensitivity with the same other parameters. On the other hand, we collect PL from various types of defects and only one of them gives rise to the ODMR contrast. This means that Γ_0 of a single defect should be larger than in ensemble experiments. Alternatively, the ODMR contrast can be sizeably increased by a proper choice of the spectral detection window[14]. Furthermore, in many sensing applications it is not necessary to use just one defect. All the silicon vacancy related defects considered here are aligned along the same axis, and, as intrinsic defects, they can be created of high concentration without need for additional doping.

III. Temperature sensing

We now discuss the temperature sensitivity, which is proportional to $(2dD/dT)^{-1} \delta v$ and therefore it is natural to select a defect with a large thermal shift β, such as the Frenkel pair V_{Si}-Si_i [Fig. 5(b)]. A large change of ZFS with temperature cannot be explained simply by thermal lattice expansion. Assuming that D is due to dipolar coupling $\propto r^{-3}$ between the silicon vacancy and the interstitial Si atom (r is the distance between them), one should have $dD/(DdT) \approx -3\alpha$. Here, $\alpha = 4.0 \times 10^{-6}$ K^{-1} is the thermal expansion coefficient of SiC, but we observe two orders of magnitude larger value of 2×10^{-3} K^{-1}. A possible explanation is that the Si interstitial (Si_i) is not rigid in the SiC lattice and a small perturbation may result in a significant shift in its position relative to V_{Si}, leading to a large change of ZFS.

The UD defect demonstrates even larger thermal shift. Using the same procedure as for the V_{Si}(V2) defect we estimate the temperature sensitivity $\delta T \sim 1 \text{ K}/\sqrt{\text{Hz}}$. Remarkably, the ODMR linewidth is significantly larger than for V_{Si}(V2) and can be explained by a high sensitivity to the local environment. In high-quality samples or for
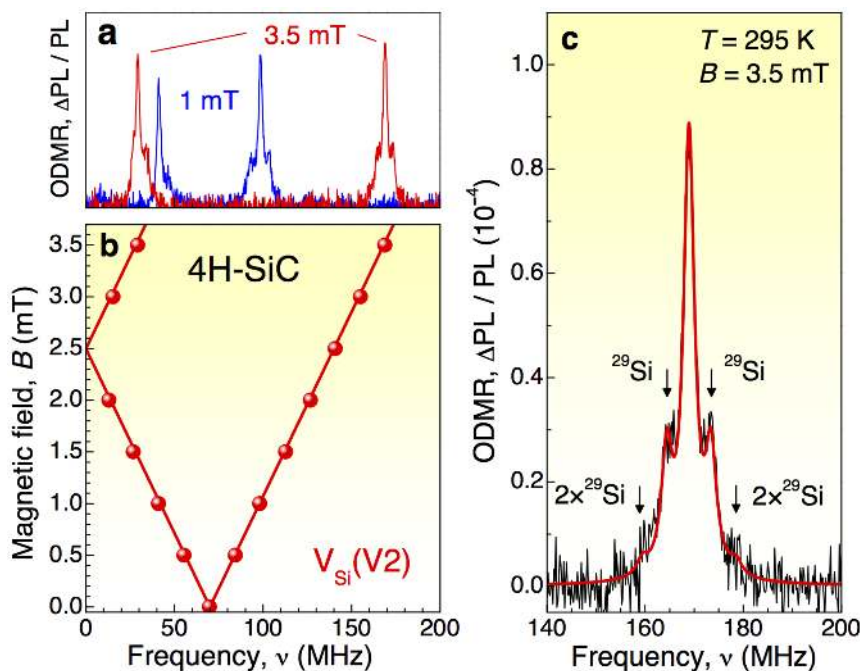
Figure 7 | Magnetic field sensing. (a) Room-temperature ODMR spectra of 4H-SiC obtained in magnetic fields $B = 1$ mT and $B = 3.5$ mT. (b) The V_{Si}(V2) ODMR frequencies as a function of magnetic field for $\mathbf{B} \parallel c$. Experimental data are shown by symbols, the solid lines correspond to the calculation as explained in the text. (c) An ODMR line of V_{Si}(V2) fitted to Eq (4). Arrows indicate the positions of the ^{29}Si isotope peaks.

single defects the inhomogeneous broadening should be suppressed, leading to homogenous linewidth $1/(\pi T_2)$. In isotopically engineered samples and with the use of advanced measurement protocols[8,12,13,17] the projected temperature sensitivity is $\delta T = 1$ mK$\left/ \sqrt{CN \cdot \text{Hz}}\right.$.

Another potential application could be a synchronized composite clock, as was originally proposed for the NV defects in diamond[37]. We find the Allan variance $(\delta\Gamma/\Gamma_0)/(2\pi Q\sqrt{\tau})$ corresponding to the resonance in Fig. 7(c) to be $2 \times 10^{-4}/\sqrt{\tau}$. By applying a spin-echo technique to isotopically purified samples it should be possible to significantly increase the quality factor $Q = \pi T_2 v_0$ and with $T_2 = 1$ ms the Allan variance approaches $10^{-8}/\sqrt{\tau}$. Further improvement by several orders of magnitude can potentially be achieved by increasing the number of defects (signal-to-noise ratio $\Gamma_0/\delta\Gamma \propto \sqrt{N}$), as this does not require intentional doping with paramagnetic impurities (i.e., nitrogen for the NV defect in diamond). In this case, the main limiting factor is temperature uncertainty. For instance, the temperature stabilization within $\Delta T = 0.01$ K leads to a fractional frequency stability $\Delta T\beta/v_0 < 10^{-6}$ for the V_{Si} defects in SiC. To compensate temperature fluctuations, it has been proposed to lock the frequency difference between two defects with different thermal shifts (β_1 and β_2), resulting in a frequency uncertainty scaled as $\sqrt{1+2(\beta_1/\Delta\beta_{1,2})^2}$ relative to the temperature-insensitive case[37]. This idea can be implemented within one SiC crystal by using different types of defects. For instance, the use of the V_{Si}(V2) defect (β_1) and the UD defect (β_2) in 6H-SiC yields $\beta_1/\Delta\beta_{1,2} < 10^{-2}$.

Summarizing, intrinsic defects in SiC demonstrate complementary properties to the NV defect in diamond. Variety of the defect characteristics makes them very perspective for various sensing applications, such as magnetometry, thermometry and chip-scale timekeeping. An important aspect is the integrability of these defects within SiC-based electronic devices[28]. Another intriguing possibility is to use biocompatibility of SiC nanocrystals to perform nanoscale magnetic field and temperature imaging in biological systems, which can be done at a fixed RF frequency as well[38].

Methods

1. Gruber, A. *et al.* Scanning Confocal Optical Microscopy and Magnetic Resonance on Single Defect Centers. *Science* **276**, 2012–2014 (1997).
2. Chernobrod, B. M. & Berman, G. P. Spin microscope based on optically detected magnetic resonance. *J. Appl. Phys.* **97**, 014903–014903–3 (2005).
3. Degen, C. L. Scanning magnetic field microscope with a diamond single-spin sensor. *Appl. Phys. Lett.* **92**, 243111 (2008).
4. Taylor, J. M. *et al.* High-sensitivity diamond magnetometer with nanoscale resolution. *Nat. Phys.* **4**, 810–816 (2008).
5. Toyli, D. M. *et al.* Measurement and Control of Single Nitrogen-Vacancy Center Spins above 600 K. *Phys. Rev. X* **2**, 031001 (2012).
6. Maze, J. R. *et al.* Nanoscale magnetic sensing with an individual electronic spin in diamond. *Nature* **455**, 644–647 (2008).
7. Balasubramanian, G. *et al.* Nanoscale imaging magnetometry with diamond spins under ambient conditions. *Nature* **455**, 648–651 (2008).
8. Toyli, D. M., de las Casas, C. F., Christle, D. J., Dobrovitski, V. V. & Awschalom, D. D. Fluorescence thermometry enhanced by the quantum coherence of single spins in diamond. *Proc Natl Acad Sci USA* **110**, 8417–8421 (2013).
9. Hall, L. T. *et al.* High spatial and temporal resolution wide-field imaging of neuron activity using quantum NV-diamond. *Sci. Rep.* **2**, 401 (2012).
10. Staudacher, T. *et al.* Nuclear Magnetic Resonance Spectroscopy on a (5-Nanometer)^3 Sample Volume. *Science* **339**, 561–563 (2013).
11. Mamin, H. J. *et al.* Nanoscale Nuclear Magnetic Resonance with a Nitrogen-Vacancy Spin Sensor. *Science* **339**, 557–560 (2013).
12. Neumann, P. *et al.* High-Precision Nanoscale Temperature Sensing Using Single Defects in Diamond. *Nano Lett.* **13**, 2738–2742 (2013).

13. Kucsko, G. *et al.* Nanometre-scale thermometry in a living cell. *Nature* **500**, 54–58 (2013).

14. Falk, A. L. *et al.* Polytype control of spin qubits in silicon carbide. *Nat. Comm.* **4**, 1819 (2013).

15. Kraus, H. *et al.* Room-temperature quantum microwave emitters based on spin defects in silicon carbide. *Nat. Phys.* **10**, 157–162 (2014).

16. Acosta, V. M. *et al.* Temperature Dependence of the Nitrogen-Vacancy Magnetic Resonance in Diamond. *Phys. Rev. Lett.* **104**, 070801 (2010).

17. Fang, K. *et al.* High-Sensitivity Magnetometry Based on Quantum Beats in Diamond Nitrogen-Vacancy Centers. *Phys. Rev. Lett.* **110**, 130802 (2013).

18. Vainer, V. S. & Il'in, V. A. Electron spin resonance of exchange-coupled vacancy pairs in hexagonal silicon carbide. *Sov. Phys. Solid State* **23**, 2126–2133 (1981).

19. Baranov, P. G. *et al.* EPR identification of the triplet ground state and photoinduced population inversion for a Si-C divacancy in silicon carbide. *JETP Lett.* **82**, 441–443 (2005).

20. Son, N. *et al.* Divacancy in 4H-SiC. *Phys. Rev. Lett.* **96**, 055501 (2006).

21. Koehl, W. F., Buckley, B. B., Heremans, F. J., Calusine, G. & Awschalom, D. D. Room temperature coherent control of defect spin qubits in silicon carbide. *Nature* **479**, 84–87 (2011).

22. Wimbauer, T., Meyer, B., Hofstaetter, A., Scharmann, A. & Overhof, H. Negatively charged Si vacancy in 4H SiC: A comparison between theory and experiment. *Phys. Rev. B* **56**, 7384–7388 (1997).

23. Sörman, E. *et al.* Silicon vacancy related defect in 4H and 6H SiC. *Phys. Rev. B* **61**, 2613–2620 (2000).

24. Mizuochi, N. *et al.* Continuous-wave and pulsed EPR study of the negatively charged silicon vacancy with S = 3/2 and C$_{3v}$ symmetry in n-type 4H-SiC. *Phys. Rev. B* **66**, 235202 (2002).

25. Baranov, P. G. *et al.* Silicon vacancy in SiC as a promising quantum system for single-defect and single-photon spectroscopy. *Phys. Rev. B* **83**, 125203 (2011).

26. Soltamov, V. A., Soltamova, A. A., Baranov, P. G. & Proskuryakov, I. I. Room Temperature Coherent Spin Alignment of Silicon Vacancies in 4H- and 6H-SiC. *Phys. Rev. Lett.* **108**, 226402 (2012).

27. Riedel, D. *et al.* Resonant Addressing and Manipulation of Silicon Vacancy Qubits in Silicon Carbide. *Phys. Rev. Lett.* **109**, 226402 (2012).

28. Fuchs, F. *et al.* Silicon carbide light-emitting diode as a prospective room temperature source for single photons. *Sci. Rep.* **3**, 1637 (2013).

29. von Bardeleben, H. J., Cantin, J. L., Henry, L. & Barthe, M. F. Vacancy defects in p-type 6H-SiC created by low-energy electron irradiation. *Phys. Rev. B* **62**, 10841–10846 (2000).

30. Childress, L. *et al.* Coherent Dynamics of Coupled Electron and Nuclear Spin Qubits in Diamond. *Science* **314**, 281–285 (2006).

31. Bradac, C. *et al.* Observation and control of blinking nitrogen-vacancy centres in discrete nanodiamonds. *Nat. Nano* **5**, 345–349 (2010).

32. Ossau, W. *et al.* Combined exciton and trion excitations in modulation doped quantum well structures. *Physica B* **298**, 315–319 (2001).

33. Bayer, M. *et al.* Fine structure of neutral and charged excitons in self-assembled In(Ga)As/(Al)GaAs quantum dots. *Phys. Rev. B* **65**, 195315 (2002).

34. Balasubramanian, G. *et al.* Ultralong spin coherence time in isotopically engineered diamond. *Nat. Materials* **8**, 383–387 (2009).

35. Hain, T. C. *et al.* Excitation and recombination dynamics of vacancy-related spin centers in silicon carbide. *J. Appl. Phys.* **115**, 133508 (2014).

36. Castelletto, S. *et al.* A silicon carbide room-temperature single-photon source. *Nature Mater.* **13**, 151–156 (2013).

37. Hodges, J. S. *et al.* Timekeeping with electron spin states in diamond. *Phys. Rev. A* **87**, 032118 (2013).

38. Babunts, R. A. *et al.* Temperature-scanned magnetic resonance and the evidence of two-way transfer of a nitrogen nuclear spin hyperfine interaction in coupled NV-N pairs in diamond. *JETP Lett.* **95**, 429–432 (2012).

Acknowledgments

Author contributions

H.K., F.F. and A.S. built up the ODMR setup; H.K., V.A.S., F.F. and D.S. collected data; P.G.B. and G.V.A. analysed the experimental data; P.G.B., V.A.S., G.V.A. and V.D. conceived the experiments; G.V.A. wrote the main manuscript text; V.D. critically reviewed and corrected the manuscript; all authors discussed the results.

Additional information